Wavefront metrology for coherent hard X-rays by scanning a microsphere

Eirik Torbjorn Bakken Skjonsfjell, Yuriy Chushkin, Federico Zontone, Nilesh Patil, Alain Gibaud, Dag W. Breiby

Wavefront metrology for coherent hard X-rays by scanning a microsphere

Eirik Torbjørn Bakken Skjønsfjell,[1] Yuriy Chushkin,[2] Federico Zontone,[2] Nilesh Patil,[1] Alain Gibaud,[3] and Dag W. Breiby[1,4,*]

[1]*Department of Physics, Norwegian University of Science and Technology, Høgskoleringen 5, 7491 Trondheim, Norway*

[2]*ESRF, The European Synchrotron, CS40220 38043 Grenoble Cedex, France*

[3]*LUMAN, IMMM, UMR 6283 CNRS, Université du Maine, Faculté des Sciences, Le Mans Cedex 09, France*

[4]*Department of Micro and Nano Systems Technology, University College of South East Norway, Raveien 197, 3184 Borre, Norway*

[*]*dag.breiby@ntnu.no*

Abstract: Characterization of the wavefront of an X-ray beam is of primary importance for all applications where coherence plays a major role. Imaging techniques based on numerically retrieving the phase from interference patterns are often relying on an a-priori assumption of the wavefront shape. In Coherent X-ray Diffraction Imaging (CXDI) a planar incoming wave field is often assumed for the inversion of the measured diffraction pattern, which allows retrieving the real space image via simple Fourier transformation. It is therefore important to know how reliable the plane wave approximation is to describe the real wavefront. Here, we demonstrate that the quantitative wavefront shape and flux distribution of an X-ray beam used for CXDI can be measured by using a micrometer size metal-coated polymer sphere serving in a similar way as the hole array in a Hartmann wavefront sensor. The method relies on monitoring the shape and center of the scattered intensity distribution in the far field using a 2D area detector while raster-scanning the microsphere with respect to the incoming beam. The reconstructed X-ray wavefront was found to have a well-defined central region of approximately 16 μm diameter and a weaker, asymmetric, intensity distribution extending 30 μm from the beam center. The phase front distortion was primarily spherical with an effective radius of 0.55 m which matches the distance to the last upstream beam-defining slit, and could be accurately represented by Zernike polynomials.

OCIS codes: (120.0120) Instrumentation, measurement, and metrology; (340.0340) X-ray optics.

References and links

1. B. C. Platt and R. Shack, "History and principles of Shack-Hartmann wavefront sensing," J. Refract. Surg. **17**(5), S573–S577 (2001).
2. A. M. Ghez, S. Salim, N. N. Weinberg, J. R. Lu, T. Do, J. K. Dunn, K. Matthews, M. R. Morris, S. Yelda, E. E. Becklin, T. Kremenek, M. Milosavljevic, and J. Naiman, "Measuring distance and properties of the milky way's central supermassive black hole with stellar orbits," Astrophys. J. **689**(2), 1044–1062 (2008).
3. J. Hartmann, *Bemerkungen über den Bau und die Justirung von Spektrographen* (Springer, 1900).
4. R. V. Shack and B. Platt, "Production and use of a lenticular Hartmann screen," in *Journal of the Optical Society of America*, (Amer Inst Physics Circulation Fulfillment Div, 500 Sunnyside blvd, Woodbury, NY 11797–2999, 1971), 656-&.
5. Y. Kohmura, Y. Nishino, T. Ishikawa, and J. Miao, "Effect of distorted illumination waves on coherent diffraction microscopy," J. Appl. Phys. **98**(12), 123105 (2005).
6. S. Le Pape, P. Zeitoun, M. Idir, P. Dhez, J. J. Rocca, and M. François, "Electromagnetic-field distribution measurements in the soft x-ray range: full characterization of a soft x-ray laser beam," Phys. Rev. Lett. **88**(18), 183901 (2002).

#258936 Received 4 Feb 2016; revised 19 Apr 2016; accepted 21 Apr 2016; published 6 May 2016

7. P. Mercère, P. Zeitoun, M. Idir, S. Le Pape, D. Douillet, X. Levecq, G. Dovillaire, S. Bucourt, K. A. Goldberg, P. P. Naulleau, and S. Rekawa, "Hartmann wave-front measurement at 13.4 nm with lambdaEUV/120 accuracy," Opt. Lett. **28**(17), 1534–1536 (2003).
8. P. Mercère, M. Idir, G. Dovillaire, X. Levecq, S. Bucourt, L. Escolano, and P. Sauvageot, "Hartmann wavefront sensor and adaptive x-ray optics developments for synchrotron applications," in *SPIE Optical Engineering + Applications*, (International Society for Optics and Photonics, 2010), 780302–780302–780311.
9. P. Mercère, M. Idir, T. Moreno, G. Cauchon, G. Dovillaire, X. Levecq, L. Couvet, S. Bucourt, and P. Zeitoun, "Automatic alignment of a Kirkpatrick-Baez active optic by use of a soft-x-ray Hartmann wavefront sensor," Opt. Lett. **31**(2), 199–201 (2006).
10. M. Idir, P. Mercere, M. H. Modi, G. Dovillaire, X. Levecq, S. Bucourt, L. Escolano, and P. Sauvageot, "X-ray active mirror coupled with a Hartmann wavefront sensor," Nucl. Instrum. Methods Phys. Res. A **616**(2-3), 162–171 (2010).
11. B. Lengeler, C. G. Schroer, M. Kuhlmann, B. Benner, T. F. Günzler, O. Kurapova, F. Zontone, A. Snigirev, and I. Snigireva, "Refractive x-ray lenses," J. Phys. D. **38**(10A), A218–A222 (2005).
12. J. M. Rodenburg, A. C. Hurst, A. G. Cullis, B. R. Dobson, F. Pfeiffer, O. Bunk, C. David, K. Jefimovs, and I. Johnson, "Hard-x-ray lensless imaging of extended objects," Phys. Rev. Lett. **98**(3), 034801 (2007).
13. P. Thibault, M. Dierolf, A. Menzel, O. Bunk, C. David, and F. Pfeiffer, "High-resolution scanning x-ray diffraction microscopy," Science **321**(5887), 379–382 (2008).
14. M. Guizar-Sicairos and J. R. Fienup, "Measurement of coherent x-ray focused beams by phase retrieval with transverse translation diversity," Opt. Express **17**(4), 2670–2685 (2009).
15. A. Robisch, K. Kröger, A. Rack, and T. Salditt, "Near-field ptychography using lateral and longitudinal shifts," New J. Phys. **17**(7), 073033 (2015).
16. M. Stockmar, M. Hubert, M. Dierolf, B. Enders, R. Clare, S. Allner, A. Fehringer, I. Zanette, J. Villanova, J. Laurencin, P. Cloetens, F. Pfeiffer, and P. Thibault, "X-ray nanotomography using near-field ptychography," Opt. Express **23**(10), 12720–12731 (2015).
17. P. Thibault, M. Dierolf, O. Bunk, A. Menzel, and F. Pfeiffer, "Probe retrieval in ptychographic coherent diffractive imaging," Ultramicroscopy **109**(4), 338–343 (2009).
18. M. Esmaeili, J. B. Fløystad, A. Diaz, K. Høydalsvik, M. Guizar-Sicairos, J. W. Andreasen, and D. W. Breiby, "Ptychographic X-ray tomography of silk fiber hydration," Macromolecules **46**(2), 434–439 (2013).
19. M. Guizar-Sicairos, S. Narayanan, A. Stein, M. Metzler, A. R. Sandy, J. R. Fienup, and K. Evans-Lutterodt, "Measurement of hard x-ray lens wavefront aberrations using phase retrieval," Appl. Phys. Lett. **98**(11), 111108 (2011).
20. E. H. Tsai, A. Diaz, A. Menzel, and M. Guizar-Sicairos, "X-ray ptychography using a distant analyzer," Opt. Express **24**(6), 6441–6450 (2016).
21. H. Quiney, A. Peele, Z. Cai, D. Paterson, and K. Nugent, "Diffractive imaging of highly focused X-ray fields," Nat. Phys. **2**(2), 101–104 (2006).
22. G. Williams, H. Quiney, A. Peele, and K. Nugent, "Fresnel coherent diffractive imaging: treatment and analysis of data," New J. Phys. **12**(3), 035020 (2010).
23. H. N. Chapman, A. Barty, S. Marchesini, A. Noy, S. P. Hau-Riege, C. Cui, M. R. Howells, R. Rosen, H. He, J. C. Spence, U. Weierstall, T. Beetz, C. Jacobsen, and D. Shapiro, "High-resolution ab initio three-dimensional x-ray diffraction microscopy," J. Opt. Soc. Am. A **23**(5), 1179–1200 (2006).
24. Y. Chushkin, F. Zontone, E. Lima, L. De Caro, P. Guardia, L. Manna, and C. Giannini, "Three-dimensional coherent diffractive imaging on non-periodic specimens at the ESRF beamline ID10," J. Synchrotron Radiat. **21**(3), 594–599 (2014).
25. S. Bérujon, E. Ziegler, R. Cerbino, and L. Peverini, "Two-dimensional X-ray beam phase sensing," Phys. Rev. Lett. **108**(15), 158102 (2012).
26. G. Porod, "Die Röntgenkleinwinkelstreuung von dichtgepackten kolloiden Systemen," Colloid Polym. Sci. **124**, 83–114 (1951).
27. H. Jiang, C. Song, C.-C. Chen, R. Xu, K. S. Raines, B. P. Fahimian, C.-H. Lu, T.-K. Lee, A. Nakashima, J. Urano, T. Ishikawa, F. Tamanoi, and J. Miao, "Quantitative 3D imaging of whole, unstained cells by using X-ray diffraction microscopy," Proc. Natl. Acad. Sci. U.S.A. **107**(25), 11234–11239 (2010).
28. D. R. Neal, J. Copland, and D. A. Neal, "Shack-Hartmann wavefront sensor precision and accuracy," in *International Symposium on Optical Science and Technology*, (International Society for Optics and Photonics, 2002), 148–160.
29. B. Honarvar Shakibaei and R. Paramesran, "Recursive formula to compute Zernike radial polynomials," Opt. Lett. **38**(14), 2487–2489 (2013).
30. R. J. Noll, "Zernike polynomials and atmospheric turbulence," J. Opt. Soc.Am. **66**(3), 207–211 (1976).
31. L. Bolloc'h, F. Livet, F. Bley, T. Schulli, M. Veron, and T. Metzger, "X-ray diffraction from rectangular slits," J. Synchro. Radiat. **9**, 258–265 (2002).
32. C. Ponchut, J. Rigal, J. Clément, E. Papillon, A. Homs, and S. Petitdemange, "MAXIPIX, a fast readout photon-counting X-ray area detector for synchrotron applications," J. Instrum. **6**(01), C01069 (2011).
33. J. Ugelstad, P. Mork, K. H. Kaggerud, T. Ellingsen, and A. Berge, "Swelling of oligomer-polymer particles. New methods of preparation," Adv. Colloid Interface Sci. **13**(1-2), 101–140 (1980).

#258936 Received 4 Feb 2016; revised 19 Apr 2016; accepted 21 Apr 2016; published 6 May 2016

34. J. Bø Fløystad, E. T. B. Skjønsfjell, M. Guizar-Sicairos, K. Høydalsvik, J. He, J. W. Andreasen, Z. Zhang, and D. W. Breiby, "Quantitative 3D X-ray imaging of densification, delamination and fracture in a micro-composite under compression," Adv. Eng. Mater. **17**(4), 545–553 (2015).
35. G. D. Smith, *Numerical Solution of Partial Differential Equations: Finite Difference Methods* (Oxford University, 1985).
36. T. Weitkamp, A. Diaz, C. David, F. Pfeiffer, M. Stampanoni, P. Cloetens, and E. Ziegler, "X-ray phase imaging with a grating interferometer," Opt. Express **13**(16), 6296–6304 (2005).
37. P. Cloetens, "Contribution to phase contrast imaging, reconstruction and tomography with hard synchrotron radiation: principles, implementation and applications," (PhD thesis, VUB (Faculteit Toegepaste Wetenschappen, Vakgroep Natuurkunde en Fotonica), 1999).

1. Introduction

Wavefront sensors are important tools used in optics, perhaps most notably in conjunction with adaptive optics for imaging extraterrestrial objects through the distortions caused by turbulence in the Earth's atmosphere [1,2]. The classical Hartmann sensor consists of an array of tiny holes in an opaque blender, projecting bright spots onto a two dimensional detector [3]. By measuring how much these spots are displaced with respect to the positions obtained for an ideal planar beam, one can measure the distortion of the incoming wave field [1]. In the refined Shack-Hartmann device, the holes are replaced by an array of small lenses [1,4], thus being more light sensitive.

Wavefront sensing is becoming increasingly important in the X-ray regime as modern X-ray sources provide bright beams with high degree of coherence used in many scattering and imaging techniques. For instance in coherent X-ray diffraction imaging (CXDI) it is critical to know how the incoming wavefront deviates from a planar beam, as deviations will reduce the quality of inverting the measured scattering patterns to real space images [5]. For soft X-rays in the 10-100 eV energy range, wavefront characterization tools similar to the (Shack-) Hartmann wavefront sensors are available [6,7]. Reverting to the Hartmann design circumvents the difficulties with refracting X-rays by first letting the X-rays pass through an array of holes, and then using a suitable fluorescent (scintillator) medium for beam detection. The visible light can then be magnified by an ordinary microscope objective and measured by a CCD camera [8]. Although this scintillator-based method has been proven to work well for measuring the wavefront for soft X-ray beams [8–10], it has the disadvantage that only relatively large beams can be measured, because multiple holes, typically in the micrometer range, must be present across the beam [8]. The resolution of these methods are generally good, and has proven to be accurate to 1/120 part of the wavelength in a study with photon energy of 92.5 eV [7]. Although Fresnel zone plates, compound refractive lenses [11] and focusing devices based on total external reflection exist, it is difficult to manufacture high-quality lenses for hard (>5 keV) X-ray imaging, because the refractive index for any material is close to unity. In addition to the technical difficulties with refracting X-rays, the beams at synchrotron facilities can be quite narrow in size, typically in the order of 0.05-100 μm to facilitate high resolution measurements. A key challenge in constructing a Shack-Hartmann wavefront sensor for X-rays is therefore to produce lenses that are small enough to accommodate an array of lenses across the beam, while still having enough refracting power to bend the X-rays sufficiently to get the angular deviation necessary for detection.

For characterizing the wavefront for X-ray beams of small lateral extent (< 5 μm), other accurate and efficient techniques have recently been developed. In ptychography [12–18] a small coherent X-ray beam (typical diameter < 5 μm) is scanned across the object, ensuring that the X-ray beam partly overlaps between neighboring exposures. From the recorded scattering patterns both the complex transmission function of the sample *and* the complex wave field of the incoming X-ray beam can be retrieved using iterative numerical methods [17]. Ptychography can also be used to measure wider wavefronts by scanning a small pinhole [19,20]. Fresnel coherent diffraction imaging has also proved to be able to retrieve the X-ray wave field [21,22], but needs a-priori knowledge of the entrance pupil of the beam (i.e. the dimensions and position of the slits shaping the beam) [22].

#258936 Received 4 Feb 2016; revised 19 Apr 2016; accepted 21 Apr 2016; published 6 May 2016

In this article we present a method of measuring the wavefront for hard X-ray beams in the tens of micrometer range which can be carried out using the experimental setup required for conventional coherent diffraction imaging experiments [23,24]. By measuring the displacement of the scattering pattern when a microscopic spherical bead is raster-scanned transversally with respect to the beam direction, we show that both the curvature of the wavefront and the intensity distribution can be retrieved, with resemblance to the work reported by Bérujon *et al.*, where the phase of the wavefront of a millimeter sized X-ray beam was measured by speckle tracking [25]. The technique has the advantages of being conceptually easy and not relying on slowly converging iterative reconstruction algorithms, and works for X-rays of high energy (> 6 keV), provided that the transverse coherence length is bigger than the sphere diameter (~3 μm).

2. Theoretical background

When a small object (200 nm – 5 μm) is exposed to coherent X-rays, a small-angle scattering pattern, caused by differences in the electron density between the sample and its surroundings, is observed in the far-field. The far-field scattering pattern intensity distribution $I(\mathbf{q})$ of a particle is proportional to the modulus square of the scattering amplitude $F(\mathbf{q})$ of the particle, $I(\mathbf{q}) \propto |F(\mathbf{q})|^2$. The scattering vector is given by $\mathbf{q} = \mathbf{k}_{out} - \mathbf{k}_{in}$, with magnitude $q = 4\pi\sin(\theta)/\lambda$. $|\mathbf{k}| = 2\pi/\lambda$ is the magnitude of the wave vectors, λ is the wavelength of the X-rays, and θ is half the scattering angle 2θ. For a sphere of radius r and volume V_p, consisting of one material, the scattering amplitude is given by [26]

$$F(q) = \rho_e V_p 3\left(\frac{\sin(qr) - qr\cos(qr)}{q^3 r^3}\right) = \rho_e P(q,r), \tag{1}$$

where $P(q, r)$ is the form factor of a uniform sphere. This can be generalized to a multilayered sphere as

$$F(q) = \rho_{e_1} P(q,r_1) + \sum_{i=2}^{n} \rho_{e_i} (P(q,r_i) - P(q,r_{i-1})), \tag{2}$$

with ρ_{ei} and r_i being the electron density and the outermost radius of the i^{th} spherical layer, respectively. By introducing the proportionality constant between the scattered intensity and the form factor, the number of scattered photons per second, $I(q)$, can be found by [27]

$$I(q) = \Phi_0 r_e^2 \, |F(q)|^2 \, \frac{A}{L^2} \tag{3}$$

Φ_0 is the incoming flux of photons [m^{-2} s^{-1}], r_e is the classical electron radius [m], A is the area of one pixel on the detector [m^2], and L is the sample detector distance [m]. Equation (3) can also be used for determining the intensity of the incoming beam, by exploiting that $|F(0)|$ equals the total number of electrons in the sample illuminated by the X-rays. The given equation for the intensity is only valid if absorption by the sample is negligible, as is the case for our spheres.

To measure accurately the apparent scattering pattern center and the total number of X-ray photons, the theoretical model given by Eq. (2) and (3) can be fitted to the experimental data. In this way, also the intensity of the central part of the scattering pattern can be estimated, which is normally hidden behind the beam stop or hard to distinguish from the direct transmitted beam. The lateral shift of the scattering pattern is then used to estimate the distortion of the wavefront.

For each scanning position of the sphere, the scattering pattern center is found in the direction normal to the local part of the wavefront (cf. Appendix for a formal statement). This is illustrated in Fig. 1 where it is emphasized that if the scattering object is laterally offset

#258936 Received 4 Feb 2016; revised 19 Apr 2016; accepted 21 Apr 2016; published 6 May 2016

within a planar wavefront, the same offset will be observed for the scattering pattern. For a non-planar wavefront, shifting the object sideways will lead to a different offset in the scattering pattern. By measuring the displacement of the scattering pattern center (x_c, y_c) compared to the position of the scattering object (x_r, y_r), one can estimate the locally averaged tangent to the wavefront. This can be expressed quantitatively by [28]

$$\begin{pmatrix} \partial W/\partial x \\ \partial W/\partial y \end{pmatrix} \approx \frac{1}{L}\begin{pmatrix} x_c - x_r \\ y_c - y_r \end{pmatrix}, \tag{4}$$

where $W(x,y)$ represents the shape of the wavefront at the coordinates x and y as given in Fig. 1 and L is the sample-detector distance. The wavefront can thus be reconstructed by direct integration

$$\begin{aligned} W_x &= \int \frac{\partial W}{\partial x} dx \\ W_y &= \int \frac{\partial W}{\partial y} dy \\ W &= W_x + W_y \end{aligned} \tag{5}$$

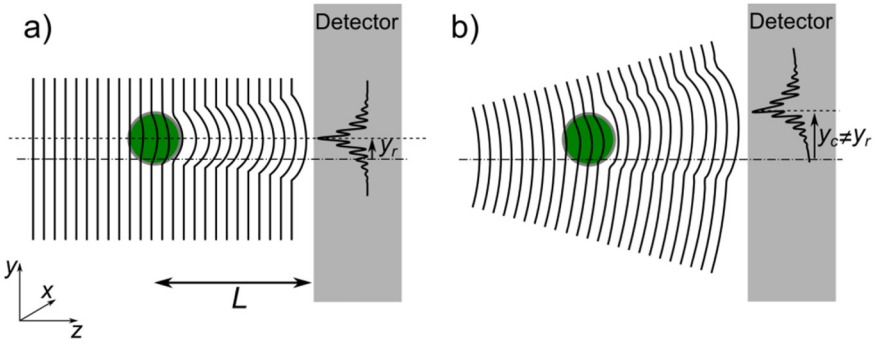

Fig. 1. Illustration of the position of the scattering pattern on the detector when the incoming wavefront is planar or curved. a) A planar wave traveling in the z-direction will be scattered by the object, generating a scattering pattern. b) When the wavefront is slightly curved, the position of the scattering pattern on the detector will depend on the local curvature of the wavefront and the sample detector distance L.

2.1 Zernike polynomials

Zernike polynomials are orthonormal functions defined on a circular domain, commonly used to parameterize the phase front of electromagnetic waves. The shape of the wavefront is then represented by Zernike coefficients which are the projection of the phase front onto the basis of Zernike polynomials. These polynomials take the form

$$\begin{aligned} Z_n^m(\rho,\varphi) &= R_n^m(\rho,\varphi)\cos(m\varphi) \\ Z_n^{-m}(\rho,\varphi) &= R_n^m(\rho,\varphi)\sin(m\varphi) \\ Z_n^0(\rho,\varphi) &= R_n^m(\rho,\varphi). \end{aligned} \tag{6}$$

Here, n and m are non-negative integers with $n \geq m$, and the radial part R_n^m is [29]

$$R_n^m(\rho) = \sum_{k=0}^{(n-m)/2} \frac{(-1)^k (n-k)!}{k!\left(\frac{n+m}{2}-k\right)!\left(\frac{n-m}{2}-k\right)!}\rho^{n-2k}, \tag{7}$$

#258936 Received 4 Feb 2016; revised 19 Apr 2016; accepted 21 Apr 2016; published 6 May 2016

for (n-m) even, and 0 for (n-m) odd. (ρ,φ) are the normalized polar coordinates of the beam. The work presented here uses Noll's sequential indices, $Z_n^m \to Z_j$ [30]. j = 1 refers to the piston term, while the classical aberration terms x-tilt, y-tilt and defocus correspond to the terms j = 2, 3 and 4, respectively.

3. Experimental details

The experiments were performed at the ID10 undulator beamline at the European Synchrotron Radiation Facility (ESRF). The partially coherent beam was produced by a Si(111) monochromator after collimation by two sets of high-power slits and focused by compound refractive lenses (CRLs) [11], located at 53.5 m from the source, at the sample position 7.5 m downstream from the CRLs. Focusing the collimated monochromatic beam resulted in a longitudinal coherence length of ~1 μm and a transverse coherence length of ~5 (25) μm in the horizontal (vertical) plane at 8.1 keV. The coherent portion of the beam was finally selected by roller-blade slits [31] with a 10 μm × 10 μm opening 55 cm upstream from the sample, providing a coherent flux of ~$2 \cdot 10^{10}$ and $5.6 \cdot 10^{10}$ photons per second at 7.0 keV (λ = 0.177 nm) and 8.1 keV (λ = 0.153 nm). The scattering patterns were collected by a Maxipix detector with 55 μm × 55 μm pixel size [32]. The intense direct beam was blocked to prevent damage to the detector by an L-shaped beam stop designed to minimize background scattering. The sketch of the experimental procedure is illustrated in Fig. 2(b). The spherical beads used were prepared by the Ugelstad method [33], and was in this case a microsphere (~3 μm diameter) of poly(methyl-methacrylate) (PMMA) with three layers of coating. By the nominal specifications, the innermost layer was a ~100 nm thick nickel coating, followed by a ~10 nm gold coating and the outermost layer was a ~50 nm SiO_2 coating, as illustrated in Fig. 2(a).

For the wavefront metrology three sets of measurements are presented, A, B and C. Measurement series B and C wwere performed with the exact same sphere in the beam. The spheres were raster scanned transversally with respect to the incoming beam as illustrated in Fig. 2 by a set of high precision translation stages having an accuracy of 50 nm. The zero position of the sphere was taken at the intensity maximum of the incoming beam. At each grid point a scattering pattern was recorded. The specific parameters for each measurement are listed in Table 1. Two different types of spheres were used for the measurements, with slightly different inner diameters as specified in Table 2. The sphere was electrostatically sticking to a 100 nm thick Si_3N_4 membrane (Silson Ltd) during the measurements.

Table 1. Experimental Parameters for the Different Measurement Series

Measurement series	Photon energy	Exposure time	Sample-detector distance L	Scan region	Step size
	keV	s	m	μm^2	μm
A	7.0	2	5.28	60 × 60	1
B	7.0	1	5.21	30 × 30	0.5
C	8.1	1	5.21	30 × 30	0.5

#258936 Received 4 Feb 2016; revised 19 Apr 2016; accepted 21 Apr 2016; published 6 May 2016

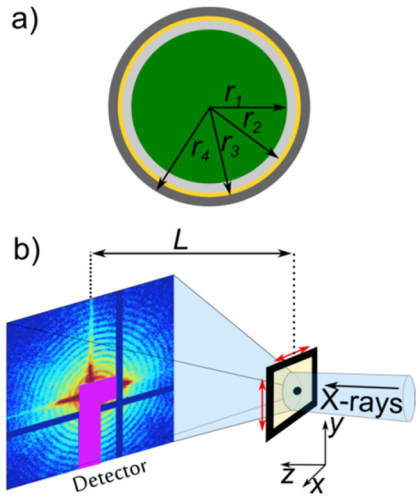

Fig. 2. The experimental setup. a) Sketch of the cross section of the microsphere. The variables r_1, r_2, r_3, r_4 denote the outer radii of the materials PMMA, nickel, gold and SiO_2. b) The metal-coated polymer sphere was placed on a silicon nitride membrane and raster-scanned perpendicularly to the X-ray beam, as indicated by the red arrows. For each position of the sphere in the beam, the corresponding scattering pattern was recorded by the 2D detector. The direct beam was blocked by a beam stop indicated with magenta color. The regions with missing data in the experimental pattern are due to gaps between detector modules and the beamstop.

4. Results and discussion

A demonstration of the key fact that the scattering pattern moves when the microsphere is laterally shifted with respect to the incoming beam is given in Fig. 3. The scattering patterns show concentric rings as expected for a scattering object having spherical symmetry. The theoretical model given by Eq. (2) and (3) was fitted to the experimental data, and the obtained parameters are given in Table 2. The radii of the different layers are fitted, while the electron densities are reported values. An example of the excellent correspondence between experimental and theoretical scattering pattern is given in Fig. 3(c) and 3(d). Note that the speckles in the experimental pattern are caused by roughness and other imperfections not accounted for in the theoretical model. It was found that for the different positions of the sphere with respect to the incoming beam, the change in the scattering patterns was to high accuracy *only* a change in the center and intensity of the scattering pattern, cf. Figure 3. Consequently, fitting the center coordinates and the intensity of the theoretical model to the experimental data, while keeping the other parameters constant, is an accurate method for finding the scattering pattern centers. Although Eq. (2) gave a good fit to the experimental data at low scattering angles, it did not fit the experimental intensity values at high angles. For these type of spheres it is known that cracks and porosity can be present in the metal coating [34], thus altering significantly the electron density distribution. A refined scattering model was therefore developed, including both the instrumental resolution (fitted to ~1.3 pixels fwhm at the detector) and imperfections in the metal coating by a static Debye-Waller factor $\exp(-\sigma^2 q^2)$ (fitted to give σ = 9.2 nm). In addition, the sharp boundaries between the different layers have been softened with a reduced electron density for the metal coating. The final electron density distribution, as function of distance from the center, of the modeled rough sphere can be seen in the inset of Fig. 3(f). Because of the lower density of the metallic coating, the radius of the outer coating had to be reduced for a better match with the experimental data. This model describes the experimental scattering, cf/ Fig. 3(f), and was used for estimating the intensity of the beam according to Eq. (3). It is not expected that the

#258936 Received 4 Feb 2016; revised 19 Apr 2016; accepted 21 Apr 2016; published 6 May 2016

theoretical model should overlap the experimental data perfectly, due to the existence of speckles in the experimental data.

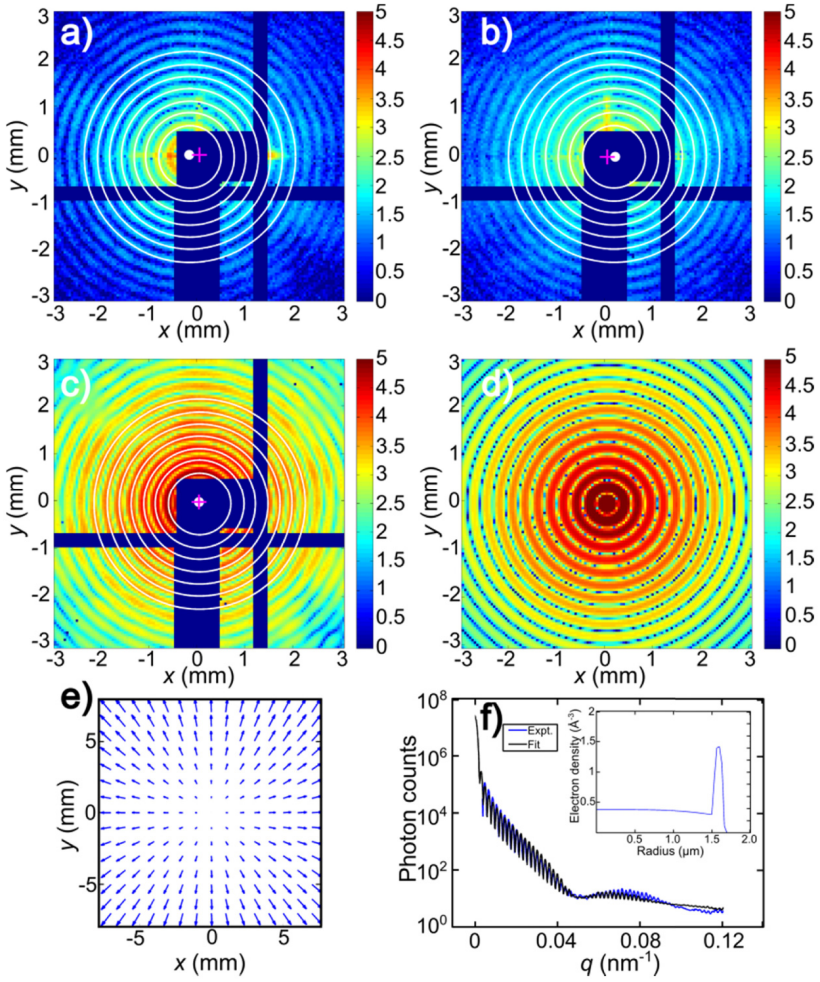

Fig. 3. Scattering patterns obtained for different sphere positions with respect to the center of the incoming beam, with the sphere displaced a) 20 μm to the left, b) 20 μm to the right, and c) at the beam center. White circles have been added to help distinguish the scattering pattern rings, with the white dot representing the scattering pattern center. The central magenta cross marks the direct beam. Note that the lateral shifts of the scattering patterns are much larger than the displacement of the sphere, being the signature of a convex wavefront. The stationary cross of enhanced background intensity is caused by slit scattering. d) The fitted scattering pattern for a centered multilayered sphere. The theoretical model is in excellent agreement with the experimental data, although there are differences caused by the fact that the wavefront and the actual microsphere have defects that give rise to speckles in the experimental pattern. The intensity scales show the photons per second in $\log_{10}$ scale. e) Vector plot illustrating the displacement of the scattering patterns for the different scanning positions close to the center. The length of the vectors is proportional to the absolute displacement $\sqrt{(x_c - x_r)^2 + (y_c - y_r)^2}$. f) Photon counts as function of q for azimuthally integrated data and the fitted model of the sphere. The beating is clear evidence for the metallic coating of the sphere. The inset shows the fitted electron density as function of radius.

#258936 Received 4 Feb 2016; revised 19 Apr 2016; accepted 21 Apr 2016; published 6 May 2016

Table 2. Fitted radii r_1 – r_4 for the Idealized Model of Eqs. (2) and (3); ρ Values are Nominal Values

Measurement series	r_1 µm	r_2 µm	r_3 µm	r_4 µm	ρ_1 Å^{-3}	ρ_2 Å^{-3}	ρ_3 Å^{-3}	ρ_4 Å^{-3}
A	1.58	1.68	1.69	1.71	0.38	2.56	4.66	0.80
B	2.26	2.36	2.37	2.44	0.38	2.56	4.66	0.80
C	2.26	2.36	2.37	2.44	0.38	2.56	4.66	0.80

Figure 3 gives clear evidence for the curvature of the wavefront. The x- and y-slopes of the wavefront along horizontal and vertical lines through the center of the beam, as calculated using Eq. (4), are shown in Fig. 4. Measurements A and B are slightly different, which is likely caused by minor alignment differences of the beamline optics (these two measurement series are separated in time by 4 months).

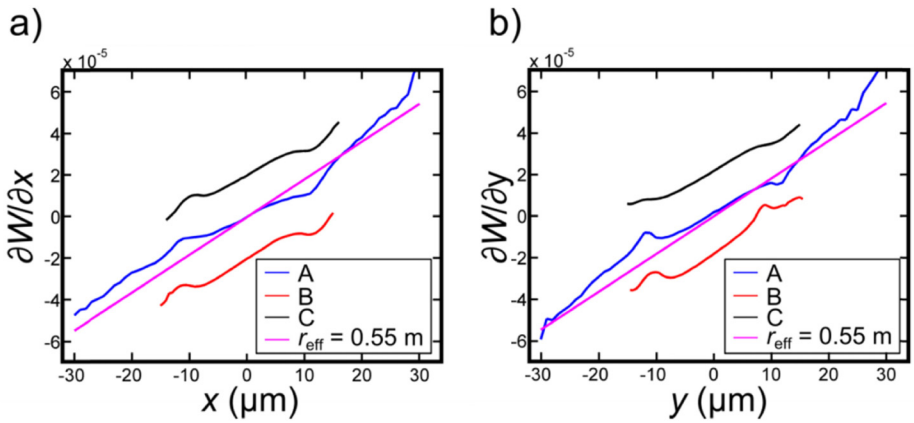

Fig. 4. Experimental data giving the wavefront slopes for the measurement series. a) Horizontal (along $y = 0$) and b) vertical (along $x = 0$) derivatives of the wavefront, through the center of the beam, as calculated using Eq. (4). The slope values for a spherical wave of radius $r_{\text{eff}} = 0.55$ m are also plotted. Measurement series B and C have been given an offset of $\pm 2 \times 10^{-5}$ for readability.

Figure 5 shows the reconstructed wavefronts, obtained by numerically integrating the measured gradients in 2D [35]. Figures 5(a)-5(c) represent the beam characteristics retrieved from measurement series A. Both the photon flux distribution, as calculated by Eq. (3), and the wavefront are plotted. Figure 5(c) shows the phase front as expressed by the 20 first Zernike polynomials, parameterizing the experimental data. The beam diameter has been assumed to be 60 µm, which is appropriate considering that the intensity drops off by several orders of magnitude further away from the center. The coefficients of the Zernike expansion are given in Fig. 6, showing that to a good approximation, the only significant coefficient is $j = 4$ ("defocus"), that is, the phase front aberration is almost exclusively spherical, with an effective radius found to be 0.55 ± 0.05 m. This radius corresponds closely to the distance from the object to the last upstream beam-defining slit. We note that a spherical wavefront in the $z = 0$ plane, corresponding to a source at $z = -R$, can be written

$$W = \sqrt{x^2 + y^2 + (z + R)^2}, \tag{8}$$

which in the paraxial limit gives $\partial W / \partial x \approx x / R$, $\partial W / \partial y \approx y / R$. The corresponding slopes for a spherical wave with $R = 0.55$ m are also plotted in Fig. 4, consistently matching the experimental data.

Figures 5(d)-5(i) show the beam characterization from measurements series B and C, which was done with a smaller step size over the central part of the beam. The intensity of the

#258936 Received 4 Feb 2016; revised 19 Apr 2016; accepted 21 Apr 2016; published 6 May 2016

beam is higher for the beam with photon energy of 8.1 keV and the phase front more symmetric, compared to the beam of 7.0 keV. The curvature is essentially spherical with effective radius r_{eff} of 0.69 ± 0.05 m and 0.65 ± 0.05 m for the 7.0 keV and 8.1 keV beam, respectively. It is noted that the wavefront is flatter (r_{eff} is larger) for the central part of the beam, than far from the center. This is also seen in Fig. 4 for measurement series A where the slope derivative has a larger value in the regions further away than 10 µm from the beam center.

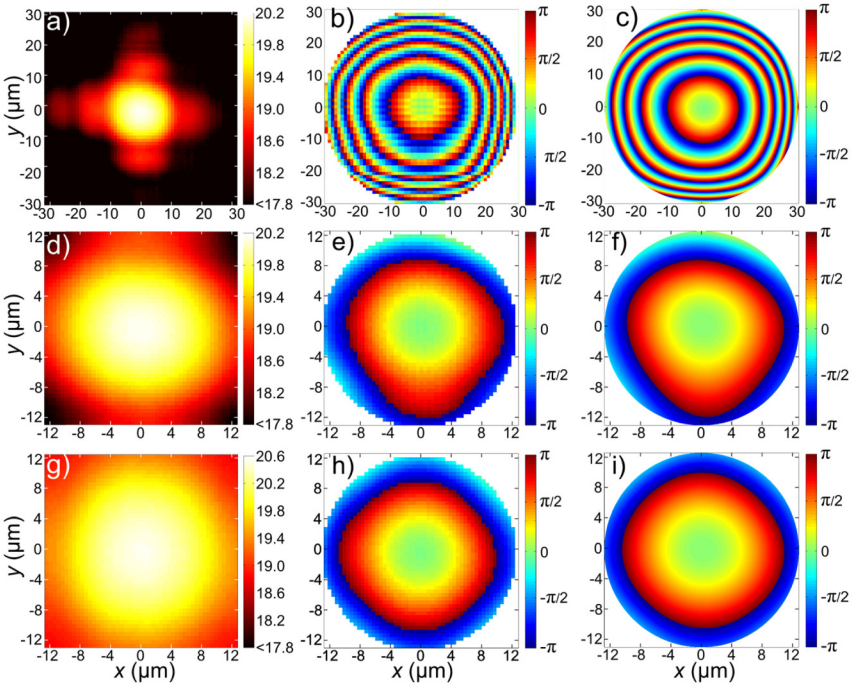

Fig. 5. Beam characterization from measurement series A, B and C. a) – f) Photon energy 7.0 keV and g) – i) Photon energy 8.1 keV. a) The $\log_{10}$ value of the photon flux in units of (photons $m^{-2}s^{-1}$), b) the measured phase front, c) a fit to the experimental data based on the 20 first Zernike polynomials, and similar for d) – f) and g) – i). It is noted that the phase front is almost the same for the two wavelengths.

The intensities from measurement series A and B are in full agreement with each other, both in magnitude and shape. The number of scattered photons in the forward direction was estimated by fitting the scattering pattern from a rough sphere to the experimental data and then using Eq. (3). From the model of the rough sphere the total number of electrons in the sample was approximately $(1.0 \pm 0.3) \cdot 10^{13}$ for the sphere used in measurement A, and $(2.3 \pm 0.3) \cdot 10^{13}$ for the sphere used in measurement B and C. The spheres absorb a fraction of the X-ray beam, but from the sphere diameter and tabulated attenuation lengths, we estimate the maximum absorption to be below 2% and therefore within the uncertainty of the calculated intensity. The total calculated number of photons was $(2.2 \pm 0.5) \cdot 10^{10}$ photons/s for the beam of 7.0 keV, close to the $2.0 \cdot 10^{10}$ photons/s previously measured. For the 8.1 keV beam the calculated number of photons was $(5.6 \pm 0.5) \cdot 10^{10}$ photons/s, which corresponds well to the previously measured $5.6 \cdot 10^{10}$ photons/s.

It is known that the polymer in the microsphere is prone to beam damage. However, the time the sphere spent in the central high intensity part of the beam is short compared to the time it takes to experience significant beam damage. In addition most of the scattered photons come from the metallic coating, which we do not expect to suffer from beam damage in any

#258936 Received 4 Feb 2016; revised 19 Apr 2016; accepted 21 Apr 2016; published 6 May 2016

significant way during the measurements. It is therefore unlikely that beam damage has had a significant influence on the accuracy of the retrieved phase fronts and intensities.

The computing time required to reconstruct the wavefront was dominated by the time needed to find the scattering symmetry center of each exposure with 1/10 pixel accuracy, amounting to almost one second. The actual integration of the wavefront, as expressed by (5), lasted only ~25 ms on a standard desktop computer (Intel i5 @ 3.30 GHz). If optimized algorithms for finding the scattering symmetry center had been implemented, we estimate that the entire reconstruction would be done in the order of seconds. Note also that the fitting routine does not require all exposures to be obtained before starting to retrieve the scattering pattern centers, effectively making the data acquisition the limiting time step. That no iterative reconstruction algorithm is used is clearly an advantage of our approach, opening for continuously updating the wavefront estimate while measuring.

The reproducibility of the presented method, which can give an indication of the accuracy, is estimated by comparing repeated wavefront measurements done shortly after each other for the same photon energies. We find that in the central region (± 4 μm from the beam center) the deviations, as obtained by subtracting reconstructed wavefronts from repeated measurements, are less than $\lambda/10$. We note that the combination of the almost perfectly spherical shape [34], the low absorption owing to the polymer core, and strong scattering by the metal coating, renders the spheres highly suitable for the beam characterization purpose. The scattering pattern centers were obtained with an accuracy of better than 0.1 pixels (5.5 μm). A suggestion for further improving the measurements would be to use a larger detector with smaller pixel size. The measured differential wavefront is necessarily the local average over the sphere, and, by using a smaller sphere, the wavefront can possibly be measured more accurately. However, a tradeoff is that a smaller sphere would scatter less, implying that the acquisition time would have to increase to maintain a sufficient signal-to-noise ratio.

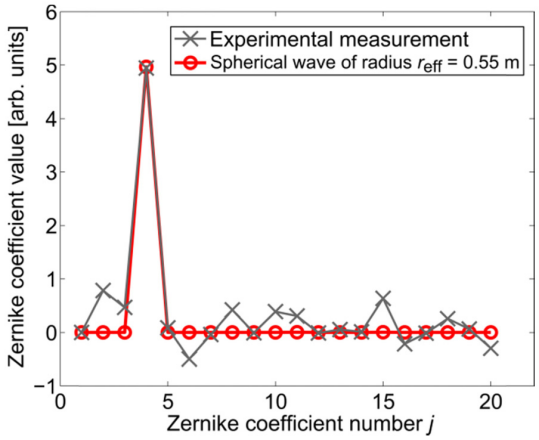

Fig. 6. Values of the 20 first Zernike coefficients used in fitting the phase front from series A, using a beam diameter of 60 μm. The defocus (j = 4) is clearly the most significant term, meaning that the wavefront deviation from a planar wave is essentially spherical. The red circles show the Zernike polynomial coefficients for a perfectly spherical wave with radius r_{eff} = 0.55 m.

It is instructive to compare our approach for wavefront reconstruction with alternative existing methods. We avoid the use of focusing lenses, and create a high intensity scattering pattern by using a strongly scattering metal-coated polymer sphere, thus giving a high signal-to-noise ratio in the scattering pattern. The sphere can in some sense be seen as a replacement for the lenses in a Shack-Hartmann wavefront sensor where the lenses are used to improve the light efficiency by focusing. Our method can in principle be performed anywhere along the optical axis and there is no need for a-priori knowledge about the beam defining optics, other

#258936 Received 4 Feb 2016; revised 19 Apr 2016; accepted 21 Apr 2016; published 6 May 2016

than the assumption that the wavefront variation is relatively slow across the scanned sphere. While an extensive literature exists also on the use of shearing interferometry and related techniques (see e.g. Weitkamp *et al* [36]), this approach requires substantial additional hardware, and is thus from our perspective less relevant for beam characterization in a dedicated CXDI setup.

We note that also ptychography has several traits similar to the approach presented here, notably that an object is transversally raster scanned in a coherent X-ray beam and that a diffraction pattern is measured at each scanning point [12]. While in most reported ptychography studies a pencil beam is probing a laterally bigger sample [13], the use of a distant analyzer (a pinhole) for reconstructing the exit wave field of a scattering object has recently been published [20]. The main difference is arguably that our method does not rely on iterative reconstruction algorithms and thus provides vastly superior reconstruction times. Moreover, our approach comes with an appealingly intuitive understanding of the reconstruction process, which might also help mitigate erroneous reconstructions. How the reconstructions compare quantitatively is a topic for further research, and it might be foreseen that the output from our approach can be further refined using ptychography, or vice versa. We emphasize that in the presented method, the wavefront is retrieved by direct integration of the measured differential wavefront. In addition, we used a 3D symmetric spherical object for which, in contrast to a pinhole, only its lateral displacement and not its rotation determines the offset of the diffraction pattern.

The described measurements for the wavefront sensing were performed with the same set up as is usually used in 3D CXDI [24]. Classical CXDI analysis assumes a planar wavefront, and one can see from the measurements that both the phase and the intensity are rather flat and uniform around the central region of the beam (± 8 μm). Still, with the curvature radius of ~55 cm, the deviation is ~1 Å (~λ) at an offset of 8 μm from the optical axis, as compared to a planar wave. It is instructive to note that for the spheres discussed in this article, the phase shift of the beam going through the central part of the sphere (with respect to air) is about 0.15λ. Consequently, it becomes clear that for the plane wave approximation to be justified, the sample diameter, the sample phase shift (i.e. the composition) and the sample centering all play vital roles. For extended or laterally offset objects with low refractive index, typically biological or organic samples giving small phase shift, the plane wave approximation might be inadequate. Conversely, for small, well centered, and strongly refracting samples, the planar approximation should hold in the case discussed here, which is consistent with the practical experience from the beamline and with the fact that the setup provides excellent resolution [24].

5. Conclusion

We have demonstrated a robust, intuitive and accurate method for measuring the wavefront. The method relies only on the use of a 2D detector, a sphere in the size range of 1 μm and a setup for raster scanning the sphere with respect to the incoming wave field. It is also required that the wavefront is relatively smooth over length scales comparable to the size of the test sphere. Our approach is closely related to the methods known as (Shack-) Hartmann wavefront sensing, but also to ptychography. Notably, it does not rely on the use of microscopic lenses, which are hard to produce for X-rays, or iterative reconstruction algorithms. The method can easily be implemented at existing coherent X-ray beamlines, essentially without modifications of the setup. The reproducibility of better than λ/10 gives highly valuable quantitative measurements of the wavefront, in terms of of both the intensity and the phase. We believe that this approach can be applied routinely to characterize wavefront distortions due to X-ray optics and alignment errors and will prove useful to further improve the performance of instruments requiring highly coherent X-ray beams.

#258936 Received 4 Feb 2016; revised 19 Apr 2016; accepted 21 Apr 2016; published 6 May 2016

Appendix

Displacement of the scattering pattern center

When the incoming X-ray wavefront irradiating the sample is curved (not planar), modifications to the scattering pattern are introduced. To describe this mathematically, the natural starting point is the Fresnel diffraction integral which propagates the wave field ψ_0 over a distance d, along z,

$$\psi_d(x,y) = e^{ikd}\frac{1}{i\lambda d}\int\int \psi_0(x_0,y_0)\exp\left\{i\frac{\pi}{\lambda d}\left[(x-x_0)^2+(y-y_0)^2\right]\right\}dx_0dy_0. \quad (9)$$

The paraxial approximation of a spherical incident wave ψ_0 is given by

$$\psi_0(\boldsymbol{\eta}) = \sqrt{I_0}\exp\left(i\pi\frac{|\boldsymbol{\eta}|^2}{\lambda r_{\text{eff}}}\right), \quad (10)$$

with intensity distribution I_0, radius of curvature r_{eff}, and wavelength λ. $\boldsymbol{\eta} = (x_0,y_0)$ is the coordinate in the sample plane. When the spherical wave passes through an object with transmission function $T(\boldsymbol{\eta})$, the wave field a distance d from the object will be [37]

$$\psi_d(\boldsymbol{\chi}) = \frac{1}{M}e^{i\frac{\pi\chi^2}{\lambda(r_{\text{eff}}+d)}}\frac{1}{i\lambda D}\int\sqrt{I_0(\boldsymbol{\eta})}T(\boldsymbol{\eta})e^{i\frac{\pi}{\lambda D}\left(\frac{\boldsymbol{\chi}}{M}-\boldsymbol{\eta}\right)^2}d\boldsymbol{\eta} \quad (11)$$

Here $\boldsymbol{\chi} = (x,y)$ is the coordinate in the detector plane, and the defocus distance D and the magnification M are given by

$$\frac{1}{D} = \frac{1}{r_{\text{eff}}}+\frac{1}{d}. \quad (12)$$

$$M = \frac{r_{\text{eff}}+d}{r_{\text{eff}}}. \quad (13)$$

If the object is laterally shifted a distance $\boldsymbol{\eta}_0$ with respect to the beam, the modified transmission function is $T' = T(\boldsymbol{\eta}-\boldsymbol{\eta}_0)$, and the wave field at the detector can be written

$$\psi'_d(\boldsymbol{\chi}) \propto \int\sqrt{I_0(\mathbf{u}+\boldsymbol{\eta}_0)}T'(\mathbf{u})e^{i\frac{\pi}{\lambda D}\left(\frac{\boldsymbol{\chi}-M\boldsymbol{\eta}_0}{M}-\mathbf{u}\right)^2}d\mathbf{u}. \quad (14)$$

Here an exchange of variables, $\mathbf{u} = \boldsymbol{\eta}-\boldsymbol{\eta}_0$, has been made. We see that the wave field will be shifted in the detector plane to have its center around $\boldsymbol{\chi}-M\boldsymbol{\eta}_0$, and if the lateral intensity distribution is approximately constant, we have

$$|\psi'_d(\boldsymbol{\chi})|^2 = |\psi(\boldsymbol{\chi}-M\boldsymbol{\eta}_0)|^2. \quad (15)$$

The shift in the detector plane is thus determined by the radius r_{eff} of the incoming wavefront at the sample position, and the sample-detector distance d. From Eq. (13) and (15) it can be deduced that the scattering pattern center will be laterally offset from the optical axis owing to the local tilt of the wavefront, as illustrated in Fig. 1.

Acknowledgment

The authors thank Helge Kristiansen of Conpart AS for supplying the microspheres used in the experiment. We also acknowledge the ESRF for providing beam time for this project. Partial funding for this work was obtained from the Norwegian PhD Network on Nanotechnology for Microsystems, which is sponsored by the Research Council of Norway, Division for Science, under contract no. 221860/F40.

#258936 Received 4 Feb 2016; revised 19 Apr 2016; accepted 21 Apr 2016; published 6 May 2016